Pergamon

Int. J. Heat Mass Transfer. Vol. 39, No. 8, pp. 1603–1615, 1996
Copyright © 1996 Elsevier Science Ltd
Printed in Great Britain. All rights reserved
0017–9310/96 $15.00+0.00

0017–9310(95)00259–6

Laminar natural convection heat transfer from isothermal spheres

H. JIA†
Department of Mechanical and Aerospace Engineering, Rutgers University, P.O. Box 909,
Piscataway, NJ 08855-0909, U.S.A.

and

G. GOGOS‡
Department of Mechanical Engineering, University of Nebraska-Lincoln,
255 Walter Scott Engineering Center, Lincoln, NE 68588-0656, U.S.A.

(*Received* 16 *June* 1994 *and in final form* 5 *July* 1995)

Abstract—Steady-state natural convection over a sphere has been studied numerically. Heat transfer and drag coefficients for a wide range of Grashof numbers ($10^1 \leqslant Gr \leqslant 10^8$) and Prandlt numbers 0.72 and 7.0 have been obtained. A plume with a mushroom-shaped front forms above the sphere whose length and thickness decrease with increasing Gr. At high Gr ($Gr \geqslant 10^7$ and $Pr = 0.72$), flow separation and an associated recirculation vortex exist in the wake of the sphere. The vortex size increases with Gr. The local Nusselt number along the sphere surface first decreases, reaches a minimum, and then increases steeply at the rear of the sphere.

1. INTRODUCTION

Studies on natural convection over a sphere are of interest in many engineering processes, such as vaporization and condensation of fuel droplets, manufacturing systems, such as in packed beds of spherical bodies for heat transfer, and in many electronic components that are nearly spherical [1]. It is also of interest for the electrodynamic balance device which may be used as a tool for studying single particle high temperature gas-solid reactions. In addition to the weight of the particle and the force due to the electric field, the vertical force due to natural convection contributes to the balance of the particle and needs to be considered while interpreting the particle weight change data [2].

Early analytical works on natural convection over a sphere have been conducted only for the limiting cases of either high Grashof number (Gr) by using boundary layer assumptions [3–8], which are invalid in the wake of the sphere, or very small Grashof number by employing asymptotic expansion techniques [9–11].

Geoola and Cornish [12] were the first to solve numerically, natural convection heat transfer over a sphere employing the full steady Navier–Stokes equations. The authors presented temperature and streamline contours, local and overall Nusselt numbers and drag coefficient (C_D) for Grashof numbers in the range $0.05 \leqslant Gr \leqslant 50$ and for Prandtl number $Pr = 0.72$. In a successive paper [13], transient results of Nusselt number and drag coefficient were presented. The study provided calculations for Grashof number up to 12 500 and Prandtl number of 0.72, 10 and 100. Their calculated temperature contours, however, did not feature the mushroom-shaped front, which has been observed experimentally [14]. Farouk [15] solved the complete steady-state Navier–Stokes equations to obtain local and overall heat transfer results for a wide range of Rayleigh numbers, $10^{-1} < Ra_D < 10^5$. Fujii *et al.* [16] provided a numerical solution of transient laminar free convection around an isothermal sphere for $Ra_D = 100$ and $Pr = 0.7$. Riley [17] obtained transient numerical solutions for $Pr = 0.72$ and 7.0 and $10^2 \leqslant Gr \leqslant 10^4$. Non-monotonic temperature profiles along the upper axis of symmetry were predicted. Dudek *et al.* [2] obtained drag coefficients both numerically and experimentally for a range of small Grashof numbers ($4 \times 10^{-4} < Gr < 0.5$).

The above brief literature review on steady-state natural convection heat transfer over a sphere, reveals that all numerical studies available in the literature have been conducted for $Gr \leqslant 10^4$. Experimental work has shown that transition to turbulence occurs at $Gr = O(10^9)$. The goal of the present work is to carry numerical simulations for Grashof number ranging up to the transition value. At these large Grashof numbers the problem becomes computationally

---

† Current address: Polymer Processing Institute, Stevens Institute of Technology, Hoboken, NJ 07030

‡ Author to whom correspondence should be addressed.

NOMENCLATURE

C_D	total drag coefficient $(F_D/\frac{1}{2}\rho v_{ref}^2 A)$
$C_{D,P}$	pressure drag coefficient
$C_{D,\mu}$	viscous drag coefficient
Gr	Grashof number $(R^2 g\beta(T_s-T_\infty)/\nu^2)$
n	number of grids
Nu	Nusselt number (hD/k)
$\bar{N}u$	overall Nusselt number
p	pressure; motion pressure
Pe	Peclet number (Dv/α)
Pr	Prandtl number (ν/α)
r	radial coordinate
r'	nondimensional radial coordinate
R	radius of the sphere
Ra	Rayleigh number $(GrPr)$
Re	Reynolds number (vD/ν)
R_ψ	relaxation factor used in GSSI
s	tangential coordinate; nondimensional tangential coordinate
t	time; nondimensional time
T	temperature
$\mathbf{v}$	velocity vector
v_{ref}	natural convection velocity $(Gr^{1/2}\nu/R)$
v	velocity
z	transformed nondimensional coordinate in r direction, where $r' = e^z - 1$.

Greek symbols

α	thermal diffusivity $= k/\rho c_p$
β	volumetric coefficient of expansion with temperature $= -1/\rho_\infty(\partial\rho/\partial T)_p$
δ_T	thermal boundary layer thickness
Δ	size of the grid
ε	convergence criterion
θ	tangential coordinate
ν	kinematic viscosity
ρ	density
ϕ	nondimensional temperature
ψ	nondimensional stream function
ω	nondimensional vorticity in azimuthal direction.

Subscripts

0	front stagnation point
D	diameter of the sphere; drag
s	surface of the sphere; dimensionless tangential coordinate
z	dimensionless radial coordinate
∞	ambient conditions.

Superscripts

$'$	dimensionless coordinates.

demanding. First, more grid points need to be clustered in the vicinity of the sphere surface to resolve the thin boundary layer. Second, contrary to the forced convection problem past a sphere where a smaller 'computational infinity' can be employed with increasing Reynolds number, in buoyancy flows resolution of the plume present in the wake of the sphere requires that the 'computational infinity' remains large. The literature [12, 13] reveals that, due to the above considerations, only results for small and moderate Grashof numbers have been reported.

With regards to experimental work, a number of studies have been conducted. In [18–21] a wide range of Grashof numbers were considered, and overall Nusselt numbers ($\bar{N}u$) were presented. Kranse and Schenk [22] studied free convection induced by the melting of a solid benzene sphere in benzene liquid. For $10^8 < Gr_D < 10^9$, they found that the local Nusselt number first decreases with θ (the tangential angle from the front stagnation point), reaches a minimum and increases thereafter. Hydrodynamic separation was observed and the separation point was found to be around 140–150°. They speculated that the separation point must coincide with the minimum in the Nusselt number. Schenk and Schenkels [23] conducted an experiment of an ice sphere melting in water. For water temperatures higher than 6°C and lower than 10°C (a temperature range within which there is no anomalous density variation and irregular flow patterns are not present) a minimum in the Nusselt number was also found and flow separation ahead of the rear stagnation point was observed.

Jaluria and Gebhart [24] investigated experimentally natural convection over an upright hemisphere in water. A rapid thickening of the boundary layer region and a sharp increase in the tangential velocity near the top of the hemisphere was reported. The Nusselt number measured decreased with θ to a minimum and then showed a sharp increase near the top of the sphere. It was observed that the heated fluid was simply realigned upward and rose in a steady, developing and axisymmetric buoyant plume. The increased velocity levels due to this realignment of the flow was given as the cause of the sharp increase in the Nusselt number near the top of the sphere. No flow reversal on the top of the sphere was observed.

Furthermore, correlations and approximate analytical methods that provide results for a wide range of Grashof or Rayleigh numbers and for all Prandtl numbers have been developed in refs. [21 and 25–27].

The goal of the present study is to solve numerically the complete Navier–Stokes equations for natural convective flow between a solid sphere and the ambient over a wide range of Grashof numbers

($10^1 \leqslant Gr \leqslant 10^8$) and for Prandtl numbers of 0.72 and 7.0. Our numerical simulations for Grashof numbers close to the critical value for transition to turbulence reveal that boundary layer separation at the top of the sphere, with associated flow reversal, does occur. The presence of the vortex is responsible for the sharp increase in the local Nusselt number near the top of the sphere. The overall Nusselt number and the drag coefficient as a function of Grashof number and profiles for local Nusselt number, pressure, vorticity and velocity components are presented.

The original motivation of this work is to study the effect of natural convection on evaporating droplets at high ambient pressures and temperatures. The present study is a first step in this research effort.

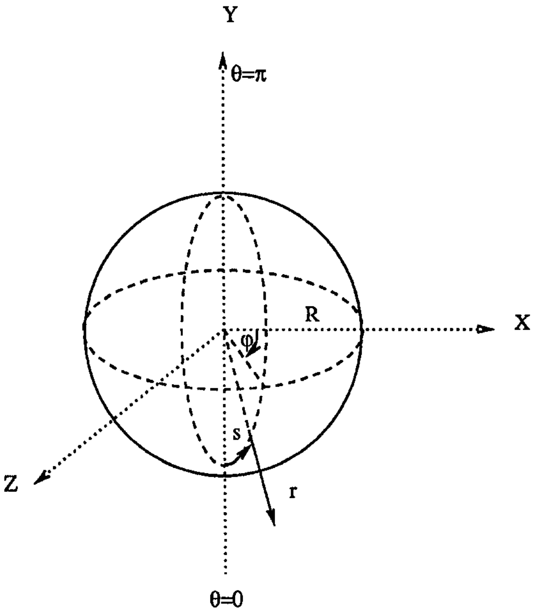

Fig. 1. The modified spherical coordinate.

2. PROBLEM FORMULATION

Natural convection around a sphere whose temperature is higher than that of its ambient is formulated next. Due to the buoyancy effect, an upward axisymmetric flow is induced near the sphere surface. At the top of the sphere, hot fluid rises and forms into an evolving plume. The Navier–Stokes equations for an incompressible fluid with constant properties, which governs such a flow field, can be written in a vector form

$$\nabla \cdot \mathbf{v} = 0 \tag{1}$$

$$\rho \frac{\partial \mathbf{v}}{\partial t} + \rho(\mathbf{v} \cdot \nabla)\mathbf{v} = -\nabla p + \mathbf{F} + \mu \nabla^2 \mathbf{v} \tag{2}$$

$$\rho c_p \frac{\partial T}{\partial t} + \rho c_p (\mathbf{v} \cdot \nabla) T = k \nabla^2 T, \tag{3}$$

where $\mathbf{v}$ is the velocity vector, $\mathbf{F}$ is the body force, ρ is the density, t is the time, p is the pressure, T is the temperature and μ, c_p and k are viscosity, heat capacity at constant pressure and thermal conductivity, respectively. Viscous dissipation has been neglected in the energy equation. The transient terms are included, since the numerical solution is obtained by a false transient algorithm.

The equations can be cast into a stream function-vorticity formulation in a modified spherical coordinate (see Fig. 1). In Fig. 1, R is the radius of the sphere, r is the normal coordinate originating from the sphere surface, s is the tangential coordinate on the surface starting from the lower stagnation point and φ is the azimuthal angle. Variables are rendered dimensionless using the following scaling parameters: R for distance, $v_{\text{ref}} = Gr^{1/2}\nu/R$ for velocities, R/v_{ref} for time and $\frac{1}{2}\rho_\infty v_{\text{ref}}^2$ for pressure. The dimensionless temperature

$$\phi = \frac{T - T_\infty}{T_s - T_\infty}.$$

In the above expressions, Gr is the Grashof number, defined as

$$\frac{R^3 g \beta (T_s - T_\infty)}{\nu^2}, \quad \beta = -\frac{1}{\rho_\infty}\left(\frac{\partial \rho}{\partial T}\right)_p$$

is the coefficient of thermal expansion of the fluid, ν is the kinematic viscosity, g is the gravitational acceleration and T_s and T_∞ are temperatures at the sphere surface and the ambient, respectively. The following coordinate transformation is introduced: $r' = r/R = e^z - 1$. In view of this transformation, using constant step size Δz, the grid points in the physical domain are clustered near the sphere surface where gradients are steep, and the outer boundary can be kept far away with a small number of grid points.

Next, the governing equations are presented in a nondimensional form. The vorticity stream function relation is given by

$$e^{2z}\omega = \frac{\partial}{\partial s}\left(\frac{1}{e^z \sin s}\frac{\partial \psi}{\partial s}\right) + \frac{\partial}{\partial z}\left(\frac{1}{e^z \sin s}\frac{\partial \psi}{\partial z}\right), \tag{4}$$

where ω is the single nonzero component of the vorticity in the azimuthal direction and ψ is the stream function which is related to the velocity components as follows:

$$v_z = -\frac{1}{e^{2z}\sin s}\frac{\partial \psi}{\partial s} \tag{5}$$

$$v_s = \frac{1}{e^{2z}\sin s}\frac{\partial \psi}{\partial z}. \tag{6}$$

The Navier–Stokes equations are converted into a vorticity transport equation in the form

$$\frac{\partial}{\partial t}(\mathrm{e}^{2z}\omega)+\frac{\partial}{\partial z}(\mathrm{e}^{z}v_z\omega)+\frac{\partial}{\partial s}(\mathrm{e}^{z}v_s\omega)$$
$$=\frac{1}{Gr^{1/2}}\frac{\partial}{\partial z}\left(\omega+\frac{\partial\omega}{\partial z}\right)+\frac{1}{Gr^{1/2}}\frac{\partial}{\partial s}\left((\cot s)\omega+\frac{\partial\omega}{\partial s}\right)$$
$$+\mathrm{e}^{z}\left(\sin s\frac{\partial\phi}{\partial z}+\cos s\frac{\partial\phi}{\partial s}\right),\quad(7)$$

where the last term is the buoyancy term. The Boussinesq assumptions have been employed in deriving this equation.

The energy equation is expressed as

$$\frac{\partial}{\partial t}(\mathrm{e}^{3z}(\sin s)\phi)+\frac{\partial}{\partial z}(\mathrm{e}^{2z}(\sin s)v_z\phi)$$
$$+\frac{\partial}{\partial s}(\mathrm{e}^{2z}(\sin s)v_s\phi)=\frac{1}{Pr\,Gr^{1/2}}\frac{\partial}{\partial z}\left(\mathrm{e}^{z}\sin s\frac{\partial\phi}{\partial z}\right)$$
$$+\frac{1}{Pr\,Gr^{1/2}}\frac{\partial}{\partial s}\left(\mathrm{e}^{z}\sin s\frac{\partial\phi}{\partial s}\right).\quad(8)$$

The above governing equations are subjected to the following boundary conditions. At the sphere surface, where $z = 0$, no-slip condition and uniform temperature are considered

$$\psi=0\quad\frac{\partial\psi}{\partial s}=0\quad\frac{\partial\psi}{\partial z}=0\quad\omega=\frac{1}{\sin s}\frac{\partial^2\psi}{\partial z^2}\quad\phi=1.\quad(9)$$

At the axis of symmetry, where $s = 0$, π, no cross flow is assumed

$$\psi=0\quad\frac{\partial\psi}{\partial z}=0\quad\omega=0\quad\frac{\partial\phi}{\partial s}=0.\quad(10)$$

At the ambient, where $z = z_\infty$, the variables of the entrained fluid are assumed those of the ambient (see next section for further discussion)

$$\psi=0\quad\omega=0\quad\phi=0.\quad(11)$$

After solutions for ϕ, ω and ψ are obtained, local and overall heat transfer and drag coefficients can be calculated by using the following formulae:

The local Nusselt number at the sphere surface is given by

$$Nu(s)=-2\frac{\partial\phi}{\partial z}.\quad(12)$$

The average Nusselt number is expressed as

$$\bar{N}u=\frac{1}{2}\int_0^\pi Nu(s)(\sin s)\,\mathrm{d}s.\quad(13)$$

Pressure at the front stagnation point is given by

$$p_0=2\int_0^\infty\phi\,\mathrm{e}^{z}\,\mathrm{d}z+\frac{4}{Gr^{1/2}}\int_0^\infty\frac{\partial\omega}{\partial s}\,\mathrm{d}z,\quad(14)$$

where the integration is carried out at $s = 0$ and p is the 'motion' pressure, namely, the difference between the actual static pressure at any location and the ambient pressure, nondimensionalized with $\frac{1}{2}\rho_\infty v_{\mathrm{ref}}^2$.

The pressure distribution along the sphere surface is given by

$$p(s)=p_0+2(1-\cos s)+\frac{2}{Gr^{1/2}}\int_0^s\left(\omega+\frac{\partial\omega}{\partial z}\right)\mathrm{d}s.\quad(15)$$

Pressure and viscous drag coefficients are expressed as

$$C_{\mathrm{D,P}}=\int_0^\pi p(s)(\sin 2s)\,\mathrm{d}s\quad(16)$$

and

$$C_{\mathrm{D},\mu}=4\int_0^\pi\omega(\sin^2 s)\,\mathrm{d}s.\quad(17)$$

The total drag coefficient is given by

$$C_{\mathrm{D}}=C_{\mathrm{D,P}}+C_{\mathrm{D},\mu}.\quad(18)$$

In the above equations, C_{D} is defined as $F_{\mathrm{D}}/\frac{1}{2}\rho v_{\max}^2A$, where F_{D} is the total dimensional drag force and A is the projected arc of the sphere (πR^2).

3. METHOD OF SOLUTIONS

The governing equations are discretized by employing a finite volume method and solved by a false transient algorithm. The only elliptic equation, equation (2.4), is solved by using a SOR algorithm [28]. Since most of the computations are performed on a Cray Y-MP, the Fortran code is vectorized to take advantage of the pipe-lined supercomputer architecture. Specifically, the SOR method is replaced by the GS-SI algorithm, which applies the Gauss–Seidel method in a spatially leapfrog pattern and can be completely vectorized [29]. Equations (7) and (8) are parabolic and are solved by the ADI method [30]. Along each of the two alternating directions, solutions are obtained by employing the Thomas algorithm [28]. The Thomas algorithm is also vectorized by storing variables in each column (r-direction) dynamically as a vector, rather than separate scalars for each row in the s-direction [31]. Then, the Do loops in the r-direction are combined within the Thomas algorithm to solve for all vectors simultaneously. Each completion of the vectorized Thomas algorithm provides solutions for the dependent variables in the whole s–r plane, which achieves maximum vectorization. The convergence criterion used in GS-SI, ε_ψ, and the criterion to check whether steady state is reached, ε_ω, are listed in Table 1. While ε_ψ is an error criterion for the entire flow field, ε_ω is a criterion for the surface vorticity at the sphere surface. The numerical integration of equations (13)–(17) is carried out by using the Simpson's rule. The spatial derivatives in equations (9), (10), (12), (14) and (15) are evaluated by the second or third-order Taylor series expansion. The

Table 1. Computing parameters used for each case ($10 \leqslant Gr \leqslant 10^8$ and $Pr = 0.72$)

	r_∞	n_r	$\Delta r\vert_s$	n_s	Δs	Δt	ε_ω	ε_ψ	R_ψ
10^1	25	80	0.041	30	6°	5×10^{-3}	5×10^{-5}	1×10^{-5}	1.8
10^2						2×10^{-2}			
10^3	16	120	0.024						
10^4									
10^5	12	160	0.016			5×10^{-2}	2×10^{-4}	5×10^{-5}	
10^6				60	3°				
10^7	8	300	7.324×10^{-3}	90	2°				
10^8		360	6.103×10^{-3}	140	1.286°				

simulations are terminated when the steady state is approached.

It is important to choose the location of the outer boundary (r_∞) properly to ensure an accurate numerical solution. The employed outer boundary conditions, equation (11), indicate that no flow crosses this boundary. Furthermore, the buoyancy plume formed at the top of the sphere needs to be well within the computational domain. The above considerations demand that r_∞ be very large. On the other hand, at a high Grashof number, and as the Grashof number increases, the boundary layer becomes much thinner. Therefore, near the surface very fine grids have to be employed in order to correctly calculate the temperature and vorticity gradients inside the boundary layer. The choice of r_∞ for each Grashof number is made after carefully balancing the above competing factors. Both the 'computational infinity' and the corresponding grid sizes for each simulation are chosen carefully by numerical tests so that all results presented in this study are independent of these choices. In addition, derivative boundary conditions at r_∞ have been tested. Regarding the flow, $\partial\psi/\partial z = 0$ is applied, and the vorticity is obtained through equation (4). For the temperature boundary condition, the outer boundary is divided into two regions. For the non-plume region ($v_z \leqslant 0$), $\phi = 0$, where as for the plume region ($v_z > 0$), the zero gradient condition, $\partial\phi/\partial z = 0$, is assumed. This kind of boundary condition allows the fluid to cross the boundary and assumes that convective heat transfer is predominant [32]. Our calculations indicate that the two different sets of boundary conditions at r_∞ have produced almost identical results for $Nu(s)$ and C_D at low Grashof numbers, as long as r_∞ is large enough. At high Grashof numbers, the local Nusselt number predicted by the two different boundary conditions are still very close, whereas C_D values differ by a small percentage. For the highest Grashof number considered (10^8), the difference in C_D reaches a maximum of 10.5%. The flow characteristics close to the sphere, such as the presence of the vortex at the top of the sphere and contours for temperature, streamlines and vorticity are the same for both sets of boundary conditions. However, far away from the sphere, the two flow fields differ substantially as expected. The flow pattern produced by using the no crossing flow boundary condition is in close resemblance to that observed experimentally in ref. [14], where streamline photos of a transient plume generated by a thermal point source are presented. It is observed that very few fluid particles move across the outer boundary. Fluid particles from the top of the plume move downward and get entrained towards the axis of symmetry. Moreover, the first kind of boundary condition is computationally less expensive and numerically more stable than the second kind. All numerical results presented in the next section have been obtained by using the first kind of boundary condition. The relevant computing parameters, such as the grid sizes (Δs, $\Delta r|_s$), the number of grids in each direction (n_s, n_r), the location of the outer boundary (r_∞), the temporal step (Δt), the convergence criteria (ε_ω, ε_ψ) and the relaxation factor (R_ψ) used in GS-SI are summarized in Table 1.

The central difference scheme is employed for $Gr \leqslant 10^2$, whereas for $Gr > 10^2$, the hybrid scheme is used. Both in this study and that of Riley [17] the central difference scheme was successfully employed for Grashof numbers up to 10^2 and 10^4, respectively. The authors in ref. [12] employed the upwind scheme for the entire range of Grashof numbers considered ($0.05 < Gr < 50$). They reported that central differencing was not stable in the outer region. For small Grashof numbers, however, diffusion dominates in the region close to the sphere surface leading to Peclet number, $Pe \ll 1$. It is well known [28, 30] that employing the upwind scheme at small Peclet numbers adds an artificial viscosity to the discretized equations.

4. RESULTS AND DISCUSSION

Extensive simulations were carried out only after the code was validated by comparing against results available in the literature. A simulation was conducted for $Gr = 25$ and $Pr = 0.72$ by employing the upwind scheme as in ref. [13]. The difference in both the Nusselt number and the drag coefficient at steady state between our simulation and that in ref. [13] is less than 1.5%. In addition, the profiles of the surface variables are in excellent agreement. However, when the upwind scheme is replaced by the central difference scheme, which is more appropriate at such a small Grashof number, for reasons discussed in detail in

Section 3, the drag coefficient predicted in our calculation is significantly smaller (13.6%) compared to that reported in ref. [13]. The validity of our model is further confirmed by the excellent agreement between the Nusselt numbers predicted in the present study and experimental studies available in the literature (see Fig. 8a and the corresponding discussion in Subsection 4.4).

Results are presented for a sphere maintained at a temperature higher than that of the ambient for $10^1 \leqslant Gr \leqslant 10^8$ and $Pr = 0.72$ and 7.0. In Subsection 4.1 characteristics of both the temperature and the flow fields are presented. The flow separation and the associated vortex in the wake of the sphere at high Grashof numbers is discussed in the next subsection. Profiles of the surface variables at different Grashof and Prandtl numbers are presented in Subsection 4.3. In the last subsection, the overall Nusselt number ($\bar{Nu}$) is compared with experimental results available in the literature, and correlations for C_D vs Gr are presented.

4.1. *Temperature and flow fields*

In Fig. 2, streamlines for $Gr = 10^2, 10^4, 10^6, 10^8$ and $Pr = 0.72$ are presented. Fluid is entrained towards the hot sphere and an upward flow is generated along the sphere surface. At the top of the sphere, hot fluid rises and forms a steady state buoyant plume. A stagnation ring is formed above the sphere, which moves downward with increasing Grashof number. Furthermore, the diameter of the ring decreases with increasing Grashof number. At low Grashof numbers most of the entrainment comes from the bottom of the sphere, whereas at high Grashof numbers it comes from the side. A similar observation has been reported by Kuehn and Goldstein [32] for natural convection over a horizontal cylinder. Figure 3 shows the temperature contours for the same Grashof and Prandtl numbers. A mushroom-shaped front is clearly indicated by the temperature contours, similar to that generated by a horizontal hot wire [33]. Both the length and the 'thickness' of the steady state plume decrease with increasing Grashof number. The thermal boundary layer thickness δ_T varies weakly along the sphere in the lower part, whereas towards the top of the sphere, it increases dramatically. Convective heat transfer becomes dominant with increasing Grashof number, and δ_T decreases substantially. For $Gr \geqslant 10^6$, δ_T becomes much smaller than R and the thin boundary layer assumption becomes applicable. However, the thin boundary layer assumption is valid only for θ up to approximately 150 and 160° for $Gr = 10^6$ and 10^8, respectively.

Figure 4 shows both the tangential and radial velocity profiles with radial distance from the sphere surface for $Gr = 10^6$ and $Pr = 0.72$. For approximately $\theta < 150°$, the tangential velocity profiles are very similar to those predicted by the boundary layer theory; they increase steeply to a maximum and then decrease steeply towards zero outside the hydrodynamic boundary layer. Furthermore, the maximum in v_θ increases with θ. However, for angles close to $\theta = \pi$, the plume begins to form. The tangential velocity profiles for these angles manifest a wider maximum due to the thickening of the boundary layer. The maximum in v_θ decreases with θ for these angles. Very close to $\theta = \pi$, the maximum in v_θ is hardly recognizable. For $\theta = 174°$, for example, v_θ first increases and then remains almost independent of the radial distance. Radial velocities are negative and of small magnitude for θ approximately less than 120°. Therefore, the range, $0 \leqslant \theta \leqslant 120°$, may be considered as the inflow region in the simulations. For higher values of θ, v_r profiles are positive and present a maximum along the radial direction, which is moving outward with further increase in θ. For even higher values of θ, such as $\theta = 174°$, v_r increases monotonically and remains level for a range of one to two radii before decaying to zero.

4.2. *Recirculation vortex on the top of a sphere*

In order to resolve both the thin boundary layers and the structure of the plume in the wake of the sphere, very fine grids had to be adopted ($\Delta\theta = 2°$ and $\Delta r|_s = 7.324 \times 10^{-3}$ for $Gr = 10^7$, and $\Delta\theta = 1.286°$ and $\Delta r|_s = 6.103 \times 10^{-3}$ for $Gr = 10^8$). The streamlines shown in Fig. 5 reveal that a small recirculation vortex and associated flow separation indeed exist in the wake of the sphere for large Grashof numbers. At $Gr = 10^7$, a very small vortex is predicted. The size of the vortex increases with Grashof number as shown for $Gr = 10^8$. In forced convective flow past a sphere, separation occurs in the wake of the sphere because fluid particles lose their momentum and are not able to overcome the adverse pressure gradient imposed by the external flow. Unlike the forced convective flow, there is no external pressure gradient imposed on the boundary layer for natural convection, since the flow is driven by the buoyancy force. Fluid particles continuously gain momentum as they translate past the sphere surface. As a result, the adverse pressure gradient which develops in the wake of the sphere and becomes steeper with increasing Grashof number (see Fig. 6a) can cause flow separation with a recirculation vortex only at extreme values of Grashof numbers. Even at $Gr = 10^8$, the axial extent of the vortex is very small. The angular extent, however, is much larger, so that the axisymmetric vortex resembles a thin cap attached to the top of the sphere, a circumstance difficult to either detect experimentally or resolve computationally. Since it has not been reported before that a vortex may be present in the wake of a sphere for natural convection heat transfer, an exhaustive examination was undertaken, to ensure that its presence is not due to some modeling deficiency. Thus, the following extensive numerical tests have been conducted for $Gr = 10^7, 10^8$ and $Pr = 0.72$: (a) the size of the grids in both directions was varied, (b) the location of the outer boundary was varied and, (c) the two different sets of boundary conditions for the outer boundary, which have been discussed in detail in Sec-

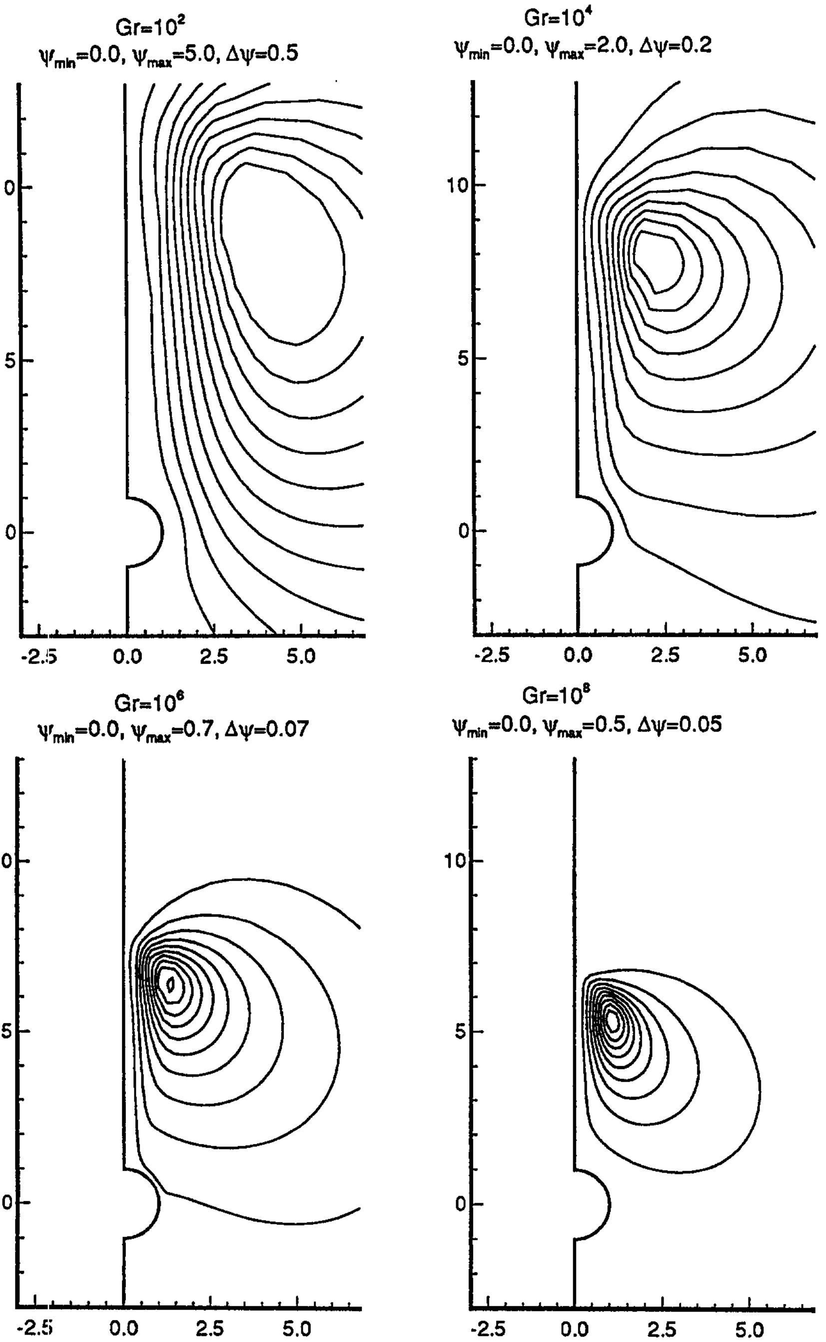

Fig. 2. Streamlines for $Gr = 10^2, 10^4, 10^6, 10^8$. $Pr = 0.72$.

tion 3, have been tested as well. It is found that for all numerical tests described above, the vortex is present and its shape, size and structure remain invariant.

4.3. *Profiles of surface pressure, vorticity and Nusselt number*

Figure 6 presents the surface pressure and vorticity distribution for $Pr = 0.72$ and 7.0. For $Pr = 0.72$, the pressure recovery in the rear of the sphere increases with Grashof number. For the high Grashof numbers considered, the adverse pressure gradient is strong enough to cause flow separation associated with a recirculation vortex in the wake of the sphere as was discussed in Subsection 4.2. For $Pr = 7.0$, the pressure variation along θ is less dramatic compared to that for $Pr = 0.72$, especially for high Grashof numbers, showing weaker pressure recovery.

At $Gr = 10^2$ and $Pr = 0.72$, the diffusive mode of

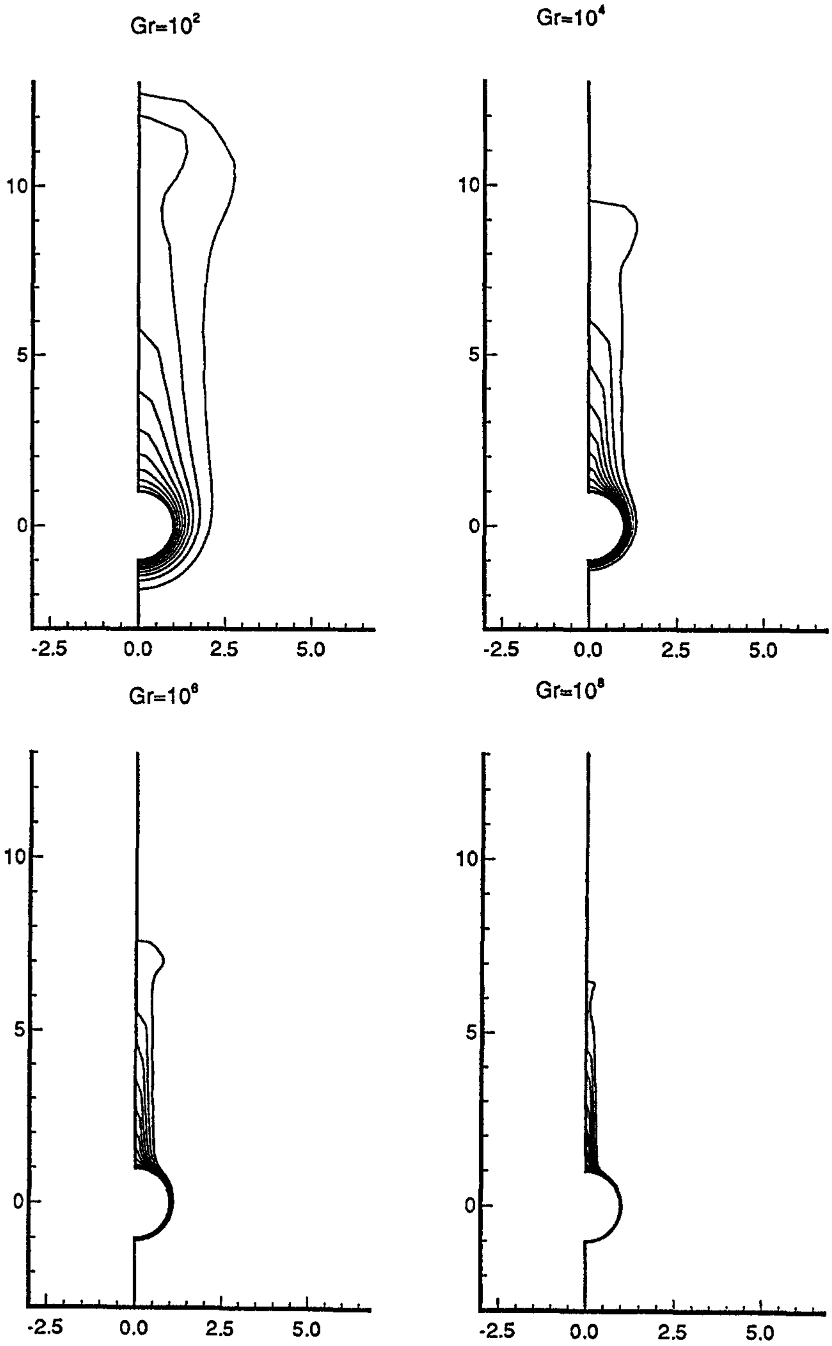

Fig. 3. Temperature contours for $Gr = 10^2, 10^4, 10^6, 10^8$. $Pr = 0.72$.

vorticity transport is predominant, as indicated by the approximately symmetric profile of the surface vorticity distribution. However, with increasing Grashof number, the convective transport of vorticity dominates. The resulting surface vorticity profiles deviate from symmetry increasingly with Grashof number. For $Gr = 10^7$ and 10^8 the surface vorticity becomes negative in the region around $\theta = \pi$, due to the vortex at the top of the sphere. For $Pr = 7.0$, even at $Gr = 10^2$ the surface vorticity profile is substantially asymmetric. At $Pr = 7.0$, negative vorticity in the rear of the sphere has not been found for Grashof numbers up to 10^7. It may appear at a higher Grashof number. However, the simulation for $Gr = 10^8$ and $Pr = 7.0$ requires even finer grids than the one for $Gr = 10^8$ and $Pr = 0.72$, due to the very thin thermal boundary

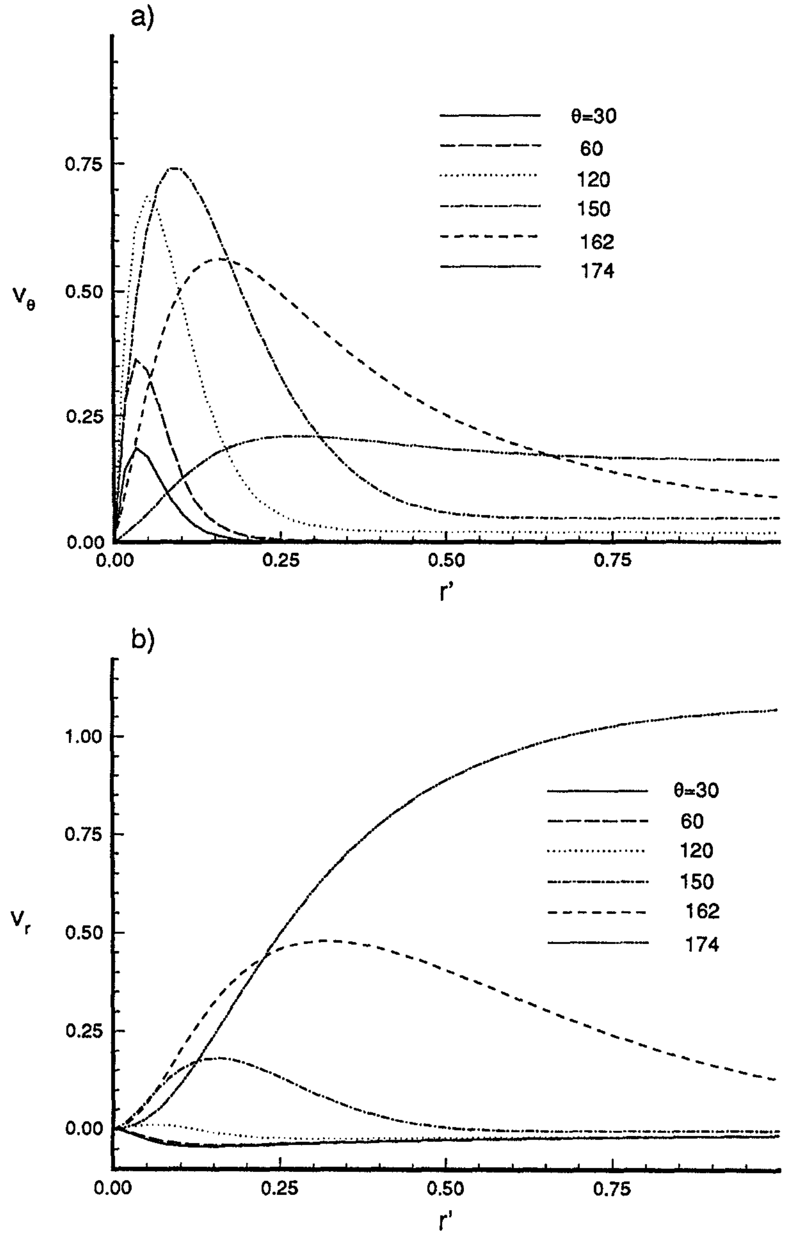

Fig. 4. (a) Tangential velocity profiles. (b) Radial velocity profiles: $Gr = 10^6$, $Pr = 0.72$.

layer. This stringent requirement makes the numerical calculation extremely intensive and has not been pursued.

Figure 7a presents the local Nusselt number as a function of θ for $Pr = 0.72$. At low and moderate Grashof number, Nusselt number decreases monotonically with θ because of the thickening of the thermal boundary layer along the sphere surface. The same trend is followed for Grashof numbers up to 10^6. However, for $Gr \geqslant 10^7$, the recirculation vortex formed in the wake of the sphere, entrains colder fluid, causing the local Nusselt number to increase with θ in the rear of the sphere after a minimum is reached. The increase is rather sharp at $Gr = 10^8$. The minimum Nu is located before the separation point. Results of the local Nusselt number for $Pr = 7.0$ are presented in Fig. 7b. The local Nusselt number decreases monotonically with θ for all Grashof numbers shown.

4.4. *Overall Nusselt number and drag coefficients*

Figure 8a shows the overall Nusselt number as a function of the Grashof number for $Pr = 0.72$ and 7.0. The present results are in very good agreement with the correlations recommended in experimental

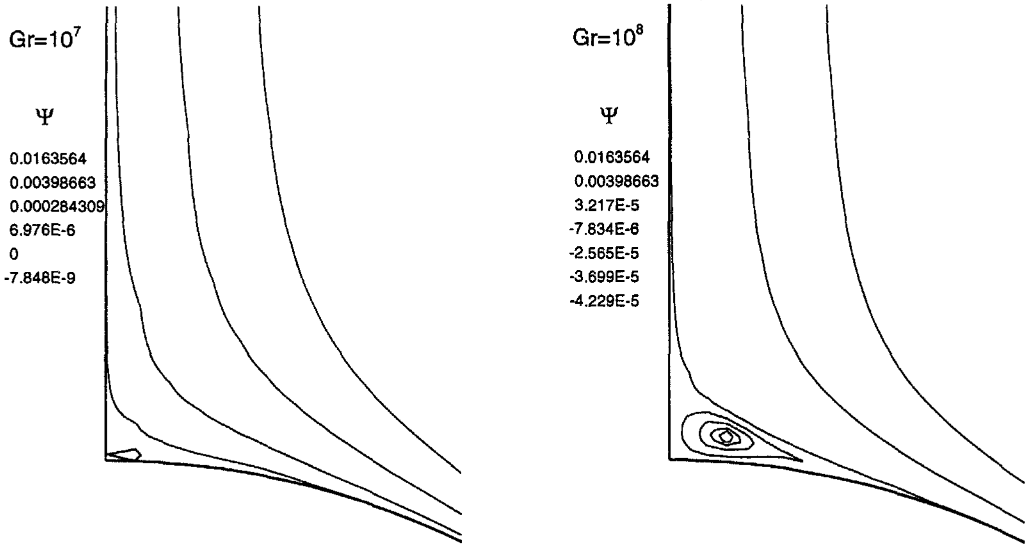

Fig. 5. Detailed flow structure (streamlines) in the wake of the sphere for $Gr = 10^7$ and 10^8. $Pr = 0.72$.

studies. Mathers *et al.* [18] have recommended $\bar{Nu} = 2+0.282(Gr_D Pr)^{1/4}$ for $Gr_D Pr \leqslant 10^2$ and $\bar{Nu} = 2+0.5(Gr_D Pr)^{1/4}$ for $10^2 \leqslant Gr_D Pr \leqslant 10^6$. Amato and Tien [20] have recommended the same correlation as that of Mathers *et al.* [18] for $3\times 10^5 \leqslant Gr_D Pr \leqslant 8\times 10^8$. The solid lines in Fig. 8a correspond to Churchill's correlation [25] which includes a more involved Prandtl number dependence in the form

$$\bar{Nu} = 2+\frac{0.589 Ra_D^{1/4}}{[1+(0.469/Pr)^{9/16}]^{4/9}}. \quad (19)$$

Table 2 provides a comparison of the numerically predicted overall Nusselt numbers ($\bar{Nu}$) with various correlations for different Grashof numbers and $Pr = 0.72$.

Figure 8b presents the viscous, pressure and total drag coefficients as a function of Grashof number for $Pr = 0.72$. At small Grashof numbers, the viscous drag is more important. The ratio of viscous drag to pressure drag is approximately 2 : 1, similar to forced convection over a sphere at small Reynolds number [34]. As the Grashof number increases, the relative contribution of pressure drag increases. At a high Grashof number, the pressure drag becomes predominant. In the case of forced convection past a sphere, C_D is insensitive to *Re* for $750 \leqslant Re \leqslant 10^5$ [34], because the surface pressure distribution, which is the predominant drag component changes remarkably little with *Re*. However, for natural convection over a sphere, C_D keeps decreasing with *Gr* due to the increase in pressure recovery with increasing Grashof number (see Fig. 6a). The total drag coefficient for $10^1 \leqslant Gr \leqslant 10^8$ has been correlated using least square regression. For $Pr = 0.72$

$$\log C_D = 1.3205-0.3753w+0.0134w^2, \quad (20)$$

where $w = \log Gr$.

For $Pr = 7.0$

$$\log C_D = 0.9011-0.2666w-0.0003w^2. \quad (21)$$

The solid line in Fig. 8b was obtained using equation (20). The square of the linear correlation coefficients in equations (20) and (21) are 0.9996 and 0.9988, respectively.

The overall Nusselt number, the viscous, pressure and total drag coefficients from all simulations in this study are presented in Table 3.

5. CONCLUSIONS

Steady-state natural convection heat transfer over a sphere whose temperature is higher than that of its ambient has been studied numerically for a wide range of Grashof numbers ($10^1 \leqslant Gr \leqslant 10^8$) and Prandtl numbers of 0.72 and 7.0.

A steady state buoyancy plume with a mushroom-shaped front, forms above the sphere whose length and thickness decrease with increasing Grashof number.

A small recirculation vortex and associated flow separation are present in the wake of the sphere for large Grashof numbers. The size of the vortex increases with increasing Grashof number and its shape resembles a thin cap attached to the top of the sphere.

The vortex is responsible for the sharp increase in the local Nusselt number near the top of the sphere.

Unlike forced convection over a sphere, where the drag coefficient is insensitive to Reynolds number over a wide range, for natural convection over a sphere, the drag coefficient keeps decreasing with increasing Grashof number due to the increase in surface pressure recovery with increasing Grashof number.

The numerically predicted overall Nusselt number is in excellent agreement with experimental results

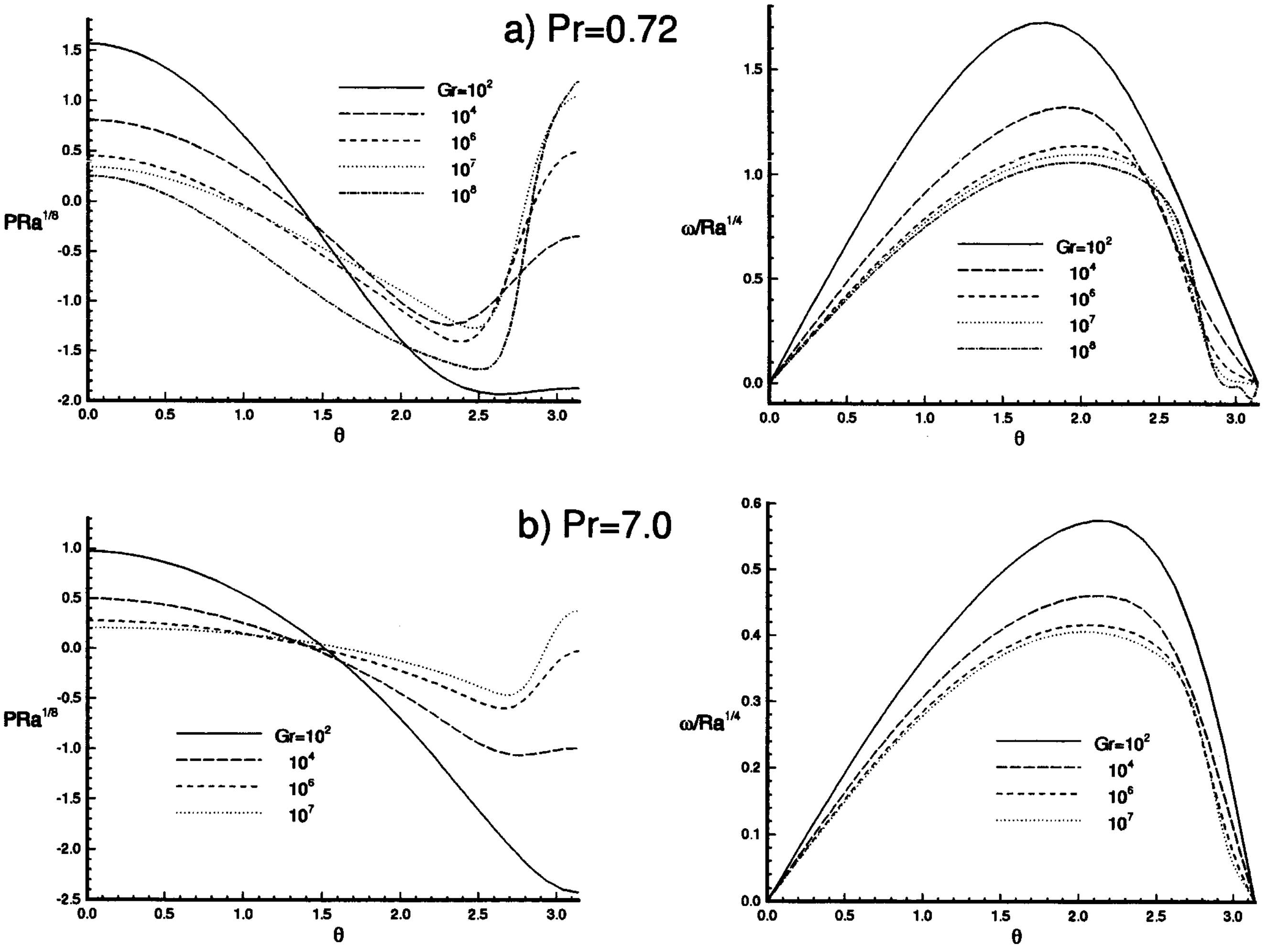

Fig. 6. Surface pressure and vorticity distribution. (a) $Pr = 0.72$. (b) $Pr = 7.0$.

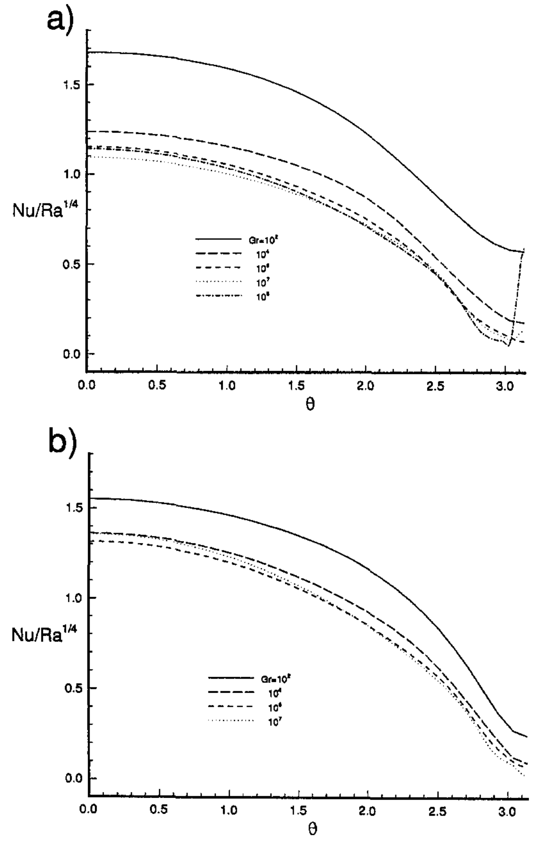

Fig. 7. Local Nusselt number distribution. (a) $Pr = 0.72$. (b) $Pr = 7.0$.

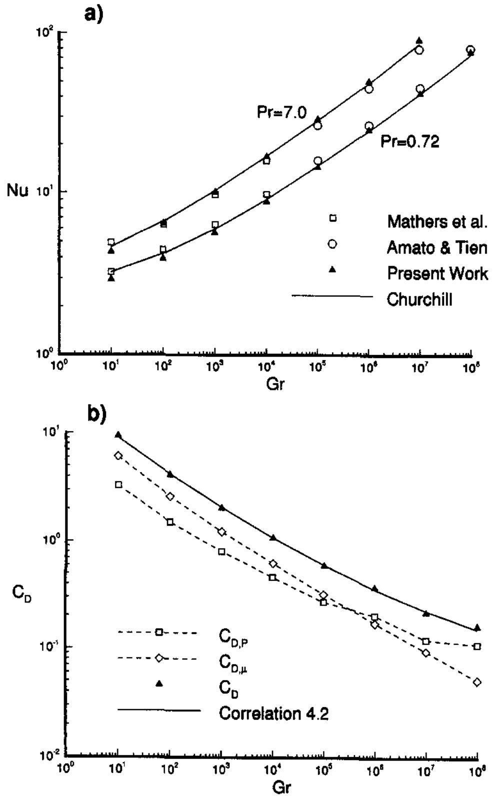

Fig. 8. (a) Overall Nusselt number as a function of Grashof number. (b) The pressure, viscous and total drag coefficients as a function of Grashof number for $Pr = 0.72$.

Table 2. Comparison of the numerically predicted overall Nusselt numbers ($\bar{Nu}$) with various correlations as a function of Grashof number for $Pr = 0.72$

	10^1	10^2	10^3	10^4	10^5	10^6	10^7	10^8
Present study	2.93	3.92	5.65	8.74	14.22	24.56	41.81	75.35
Mathers *et al.* [18]	3.26	4.45	6.36	9.75	15.77	26.49	45.56	79.46
Hassani *et al.* [21]	3.26	4.24	5.98	9.07	14.57	24.35	41.75	72.69
Raithby *et al.* [26]	3.27	4.26	6.02	9.14	14.70	24.59	42.17	73.44
Jafarpur *et al.* [27]	3.26	4.25	6.00	9.11	14.64	24.48	41.98	73.10

Table 3. Overall Nusselt number ($\bar{Nu}$), pressure ($C_{D,P}$), viscous ($C_{D,\mu}$) and total (C_D) drag coefficients for $10^1 \leqslant Gr \leqslant 10^8$ and $Pr = 0.72$ and 7.0.

		10^1	10^2	10^3	10^4	10^5	10^6	10^7	10^8
$Pr = 0.72$	$\bar{Nu}$	2.93	3.92	5.65	8.74	14.22	24.56	41.81	75.35
	$C_{D,P}$	3.27	1.51	0.80	0.46	0.27	0.20	0.12	0.109
	$C_{D,\mu}$	6.07	2.60	1.23	0.62	0.32	0.17	0.094	0.051
	C_D	9.34	4.11	2.03	1.08	0.59	0.37	0.214	0.160
$Pr = 7.0$	$\bar{Nu}$	4.32	6.41	10.01	16.72	28.74	49.85	89.62	
	$C_{D,P}$	1.87	0.88	0.47	0.27	0.15	0.078	0.043	
	$C_{D,\mu}$	3.31	1.50	0.74	0.39	0.21	0.112	0.062	
	C_D	5.18	2.38	1.21	0.66	0.36	0.190	0.105	

available in the literature. Correlations for the drag coefficient are presented over a wide range of Grashof numbers.

Acknowledgements—Computational work was performed on the NSF National Center for Supercomputing Applications at the University of Illinois at Urbana-Champaign under grant no. CBT920039N. The support of this computing facility is greatly appreciated.

REFERENCES

1. B. Gebhart, Y. Jaluria, R. L. Mahajan and B. Sammakia, *Buoyancy-Induced Flows and Transport*, p. 212. Hemisphere Publishing Corporation, New York (1988).
2. D. R. Dudek, T. H. Fletcher, J. P. Longwell and A. F. Sarofim, Natural convection induced drag forces on spheres at low Grashof numbers: comparison of theory with experiment, *Int. J. Heat Mass Transfer* **31,** 863–873 (1988).
3. H. J. Merk and J. A. Prins, Thermal convection in laminary boundary layers, *Appl. Sci. Res.*, Series A **4,** 11–24 (1953).
4. H. J. Merk and J. A. Prins, Thermal convection in laminary boundary layers, *Appl. Sci. Res.*, Series A **4,** 195–206 (1954).
5. H. J. Merk and J. A. Prins, Thermal convection in laminary boundary layers, *Appl. Sci. Res.*, Series A **4,** 207–221 (1954).
6. A. Acrivos, A theoretical analysis of laminar natural convection heat transfer to non-Newtonian fluids, *AIChE J.* **6,** 584–590 (1960).
7. T. Chiang, A. Ossin and C. L. Tien, Laminar free convection from a sphere, *J. Heat Transfer* **86,** 537–542 (1964).
8. J. M. Potter and N. Riley, Free convection from a heated sphere at large Grashof number, *J. Fluid Mech.* **100,** 769–783 (1980).
9. F. E. Fendell, Laminar natural convection about an isothermal heated sphere at small Grashof number, *J. Fluid Mech.* **34,** part 1, 163–176 (1968).
10. A. Hossain and B. Gebhart, Natural convection about a sphere at low Grashof number, *Heat Transfer IV, Proceedings of International Heat Transfer Conference*, NC 1.6, (1970).
11. S. N. Singh and M. M. Hasan, Free convection about a sphere at small Grashof number, *Int. J. Heat Mass Transfer* **26,** 781–783 (1983).
12. F. Geoola and A. R. H. Cornish, Numerical solution of steady state free convective heat transfer from a solid sphere, *Int. J. Heat Mass Transfer* **24,** 1369–1379 (1981).
13. F. Geoola and A. R. H. Cornish, Numerical simulation of free convective heat transfer from a sphere, *Int. J. Heat Mass Transfer* **25,** 1677–1687 (1982).
14. D. J. Shlien and R. L. Boxman, Laminar starting plume temperature field measurement, *Int. J. Heat Mass Transfer* **24,** 919–931 (1981).
15. B. Farouk, Natural convection heat transfer from an isothermal sphere, *Therm. Sci.* **16,** 347–364 (1983).
16. T. Fujii, T. Honda and M. Fujii, A numerical analysis of laminar free convection around an isothermal sphere: finite-difference solution of the full Navier–Stokes and energy equations between concentric spheres, *Numer. Heat Transfer* **7,** 103–111 (1984).
17. N. Riley, The heat transfer from a sphere in free convective flow, *Comput. Fluids* **14,** 225–237 (1986).
18. W. G. Mathers, A. J. Maddern Jr and E. L. Piret, Simultaneous heat and mass transfer in free convection, *Ind. Engng Chem.* **49,** 961–968 (1957).
19. T. Yuge, Experiments on heat transfer from spheres including combined natural and forced convection, *J. Heat Transfer* **82,** 214–220 (1960).
20. W. S. Amato and C. Tien, Free convection heat transfer from isothermal spheres in water, *Int. J. Heat Mass Transfer* **15,** 327–339 (1972).
21. A. V. Hassani and K. G. T. Hollands, On natural convection heat transfer from three-dimensional bodies of arbitrary shape, *J. Heat Transfer* **111,** 363–371 (1989).
22. A. A. Kranse and J. Schenk, Thermal free convection from a solid sphere, *Appl. Sci. Res.* **15,** 397–403 (1965).
23. J. Schenk and F. A. M. Schenkels, Thermal free convection from an ice sphere in water, *Appl. Sci. Res.* **19,** 465–476 (1968).
24. Y. Jaluria and B. Gebhart, On the buoyancy-induced flow arising from a heated hemisphere, *Int. J. Heat Mass Transfer* **18,** 415–431 (1975).
25. S. W. Churchill, Comprehensive theoretically based, correlating equations for free convection from isothermal spheres, *Chem. Engng Commun.* **24,** 339–352 (1983).
26. G. D. Raithby and K. G. T. Hollands, A general method of obtaining approximate solutions to laminar and turbulent free convection problems, *Adv. Heat Transfer* **11,** 266–315 (1975).
27. K. Jafarpur and M. M. Yovanovich, Laminar free convective heat transfer from isothermal sphere: a new analytical method, *Int. J. Heat Mass Transfer* **35,** 2195–2201 (1992).
28. S. V. Patankar, *Numerical Heat Transfer and Fluid Flow*, pp. 56–57; 52–53; 61–62; 85–86. Hemisphere, New York (1980).
29. D. M. Young, *Iterative Solution of Large Linear Systems*, pp. 367–372. Academic Press, San Diego (1971).
30. P. J. Roache, *Computational Fluid Dynamics*, pp. 91–94; 64–67. Hermosa Albuquerque, NM (1976).
31. C. H. Chuan and W. C. Schreiber, The simulation of convective solidification using 3-D computer code vectorized for optimum performance on supercomputers in *Science and Engineering on Supercomputers* (Edited by E. C. Pitcher), pp. 431–442. Computational Mechanics Publications; Springer, New York (1990).
32. T. H. Kuehn and R. J. Goldstein, Numerical solution to the Navier–Stokes equations for laminar natural convection about a horizontal isothermal circular cylinder, *Int. J. Heat Mass Transfer* **23,** 971–979 (1980).
33. C. M. Vest and M. L. Lawson, Onset of convection near a suddenly heated horizontal wire, *Int. J. Heat Mass Transfer* **15,** 1281–1283 (1972).
34. R. Clift, J. R. Grace and M. E. Weber, *Bubbles, Drops and Particles*, pp. 108; 122. Academic Press, New York (1978).